

Article

# Hydrothermal Synthesis of Iridium-Substituted NaTaO<sub>3</sub> Perovskites

David L. Burnett<sup>1</sup>, Christopher D. Vincent<sup>1</sup>, Jasmine A. Clayton<sup>1</sup>, Reza J. Kashtiban<sup>2</sup> and Richard I. Walton<sup>1,\*</sup>

<sup>1</sup> Department of Chemistry, University of Warwick, Coventry CV4 7AL, UK; d.burnett@bham.ac.uk (D.L.B.); cdv1230@gmail.com (C.D.V.); jasmine.clayton@warwick.ac.uk (J.A.C.)

<sup>2</sup> Department of Physics, University of Warwick, Coventry CV4 7AL, UK; r.jalilikashtiban@warwick.ac.uk

\* Correspondence: r.i.walton@warwick.ac.uk

**Abstract:** Iridium-containing NaTaO<sub>3</sub> is produced using a one-step hydrothermal crystallisation from Ta<sub>2</sub>O<sub>5</sub> and IrCl<sub>3</sub> in an aqueous solution of 10 M NaOH in 40 vol% H<sub>2</sub>O<sub>2</sub> heated at 240 °C. Although a nominal replacement of 50% of Ta by Ir was attempted, the amount of Ir included in the perovskite oxide was only up to 15 mol%. The materials are formed as crystalline powders comprising cube-shaped crystallites around 100 nm in edge length, as seen by scanning transmission electron microscopy. Energy dispersive X-ray mapping shows an even dispersion of Ir through the crystallites. Profile fitting of powder X-ray diffraction (XRD) shows expanded unit cell volumes (orthorhombic space group *Pbmm*) compared to the parent NaTaO<sub>3</sub>, while XANES spectroscopy at the Ir L<sub>III</sub>-edge reveals that the highest Ir-content materials contain Ir<sup>4+</sup>. The inclusion of Ir<sup>4+</sup> into the perovskite by replacement of Ta<sup>5+</sup> implies the presence of charge-balancing defects and upon heat treatment the iridium is extruded from the perovskite at around 600 °C in air, with the presence of metallic iridium seen by in situ powder XRD. The highest Ir-content material was loaded with Pt and examined for photocatalytic evolution of H<sub>2</sub> from aqueous methanol. Compared to the parent NaTaO<sub>3</sub>, the Ir-substituted material shows a more than ten-fold enhancement of hydrogen yield with a significant proportion ascribed to visible light absorption.

**Keywords:** perovskite; tantalate; crystallisation; nanocrystals; photocatalysis; water splitting

**Citation:** Burnett, D.L.; Vincent, C.D.; Clayton, J.A.; Kashtiban, R.J.; Walton, R.I. Hydrothermal Synthesis of Iridium-Substituted NaTaO<sub>3</sub> Perovskites. *Nanomaterials* **2021**, *11*, 1537. <https://doi.org/10.3390/nano11061537>

Academic Editors: Gimyeong Seong, Juan Carlos Rendón-Angeles and Yoon-Bong Hahn

Received: 30 April 2021

Accepted: 7 June 2021

Published: 10 June 2021

**Publisher's Note:** MDPI stays neutral with regard to jurisdictional claims in published maps and institutional affiliations.



**Copyright:** © 2021 by the author. Licensee MDPI, Basel, Switzerland. This article is an open access article distributed under the terms and conditions of the Creative Commons Attribution (CC BY) license (<http://creativecommons.org/licenses/by/4.0/>).

## 1. Introduction

The hydrothermal synthesis of ABO<sub>3</sub> perovskite oxides has attracted a large amount of interest in the past decade [1]. This includes families of materials with important properties such as titanates (B = Ti) with dielectric properties [2], piezoelectric zirconate-titanates (B = Zr, Ti) [3], multiferroic chromites (B = Cr) [4], and ferrites (B = Fe) with applications in redox catalysis [5]. The synthesis of this range of compositions work builds on a body of literature on hydrothermal crystallisation of one of the prototypical perovskites BaTiO<sub>3</sub> [6]. The attraction of the hydrothermal synthesis method lies in the use of solution chemistry to enable crystallisation from solution directly at mild temperatures typically less than 200 °C: this allows adjustment of the crystal morphology, including size and shape of crystallites on the nanoscale, as well as the possibility of isolating compositions not stable under more extreme conditions [7–12]. This level of control in the synthesis of oxide materials is lacking in traditional high temperature routes, and even in co-precipitation or sol-gel approaches, in which a firing step is needed to induce crystallinity; this means annealing takes place, with control of crystallite size being difficult to achieve.

Many functional oxide materials have been accessed via hydrothermal synthesis routes, some with unique properties arising from their nanostructure. A notable example is the formation of nanowires of Cu<sub>2</sub>O that have considerably enhanced photoactivity in the visible region of the spectrum [13]. The hydrothermal method also provides a

convenient method for the formation of composite materials, where the growth of an oxide on a support in situ provides new functional solids with exceptional properties. Examples include the formation of graphene oxide conjugated Cu<sub>2</sub>O nanowires for gas sensing [14], ammonia sensing from Cu<sub>2</sub>O nanoparticles decorated with MoS<sub>2</sub> nanosheets [15], and graphene oxide–MnO<sub>2</sub> nanocomposites for supercapacitors [16].

Niobate and tantalate perovskites, ANbO<sub>3</sub> and ATaO<sub>3</sub> where A = Na or K, have attracted much attention due to their practical applications in two important areas: as potential lead-free electroceramics, as end-members of the piezoelectric material K<sub>0.5</sub>Na<sub>0.5</sub>NbO<sub>3</sub>, and as photocatalysts for applications such as water splitting and carbon dioxide conversion. Hydrothermal synthesis of these materials has been extensively investigated and the pathways during the formation of the perovskite products have been mapped [17–19]. Some control of crystallite morphology has proved possible; for example, it has been shown that a low concentration of Nb<sub>2</sub>O<sub>5</sub> as a precursor leads to nanorods or nanoplates of NaNbO<sub>3</sub>, while a lower concentration of NaOH yields cubes [20]. Crystallite morphology of NaNbO<sub>3</sub> can also be influenced by the choice of niobium oxide precursor [21], the pH of the solution [22], and the choice of solvent [23]. For electroceramics, fine-grained ceramics can be produced by annealing the powders from hydrothermal reactions: piezoelectric ceramics formed from hydrothermally prepared alkali niobates and tantalates have shown characteristics comparable to ceramics made by conventional methods, but with the advantage of lower sintering temperatures to achieve densification [24–26]. For photocatalysis, the high surface areas of the nanostructured crystallites offers high reactivity; for example, Shi et al. prepared nanocubes and compared them with nanowires, and found a correlation between crystal shape and photocatalytic activity for hydrogen evolution from water/methanol [27]. High surface areas are also useful for support materials for co-catalysts.

In photocatalysis, NaNbO<sub>3</sub> and NaTaO<sub>3</sub> are typically doped with substituent metals to tune their band gaps, and then used as supports for precious metals with the particular aim to permit absorption of visible light [28]. Doping of perovskite oxides with precious metal cations is of more general interest, but can present a synthetic challenge as there is a strong tendency for the precious metal substituent to be reduced to the elemental state, even upon heating in air. LaCr<sub>1-x</sub>M<sub>x</sub>O<sub>3</sub> (LCMO) ( $x = 0.01, 0.05, 0.10$  with M = Pd, Co, Ir) materials were prepared using conventional solid-state synthesis from single metal oxide precursors at 1200 °C, with a reduction in band gap observed for all substituted materials [29]. Rh-doped BaTiO<sub>3</sub> nanoparticles, with 2% of the substituent, were prepared by a co-precipitation route using oxalate as solution additive at temperatures between 700 and 900 °C [30]. The Rh was found in the +3 oxidation state and on heating to higher temperatures the rhodium was lost, with phase transformation of the perovskite. 0.5% iridium-doped SrTiO<sub>3</sub> was prepared by a solid-state method, and in a second step under reducing conditions, exsolution of the Ir was found that resulted in supported Ir nanoparticles, embedded in the oxide support, showing little agglomeration when used in CO oxidation catalysis [31]. Ir-doped SrTiO<sub>3</sub> (1–5% Ir) has also been studied for photocatalysis, and the oxidation state of the Ir was found to dictate the properties towards photocatalytic water splitting, with Ir<sup>4+</sup> giving the most favourable properties [32]. Kudo et al. studied a number of precious-metal-doped perovskites for photocatalytic water splitting; in the case of NaNbO<sub>3</sub> and NaTaO<sub>3</sub>, prepared by a solid-state method, doping with Ir or Rh creates band gaps suitable for visible light absorption when co-doped with alkaline earth or lanthanide cations, Ba and La, respectively [33,34].

Given the need for convenient synthesis methods for precious-metal-substituted perovskites, which may also allow control of the substituent oxidation state, we have investigated the use of hydrothermal reaction conditions. In this paper we consider the possibility of iridium substitution in NaTaO<sub>3</sub> by a direct hydrothermal synthesis and show that a one-step crystallisation is able to form nanocubes with homogeneous distribution of iridium, as proven by various experimental techniques. We chose this composition to study since there is already a body of work on the hydrothermal synthesis of NaTaO<sub>3</sub>, and

the case of iridium substitution has been reported by other synthesis methods, which provide a comparison to the milder solution conditions. To our knowledge, the inclusion of precious metal substituents in an oxide perovskite host by hydrothermal synthesis has not yet been reported. Our aim was to explore the maximum level of inclusion of the precious metal in the perovskite host structure to test the synthetic strategy. We present an assessment of the use of the materials as visible light photocatalysts for hydrogen evolution from water.

## 2. Materials and Methods

### 2.1. Materials Synthesis

Chemicals used were sourced from chemical companies: Ta<sub>2</sub>O<sub>5</sub> (Alfar Aesar, Heysham, UK, 99%), hydrated IrCl<sub>3</sub> (Johnson Matthey, London, UK, 52.29% Ir), NaOH (Fisher Scientific, Loughborough, UK, Laboratory Grade) and H<sub>2</sub>O<sub>2</sub> (Sigma Aldrich, Gillingham, UK, 30% in water by volume). The substituted tantalates were synthesised by the reaction of 1.1 mmol tantalum (V) oxide in 10 mL of 10 M NaOH in 40 vol% H<sub>2</sub>O<sub>2</sub>, with a portion of the oxide replaced by a chosen amount of iridium (III) chloride. The use of H<sub>2</sub>O<sub>2</sub> as an oxidant was based on our previous work on hydrothermal synthesis of iridium oxides to prevent the formation of metallic iridium [35]. After stirring the reagents for one hour in a 20 mL polytetrafluoroethylene container, the reaction mixture was sealed in a steel autoclave and heated at 240 °C for three days. After cooling naturally to room temperature, the powders were collected via vacuum filtration, and washed with 20 mL of 3 M HNO<sub>3</sub>, followed by 20 mL of acetone, and then dried in air at 70 °C before further study.

### 2.2. Characterisation

Powder X-ray diffraction (XRD) data were recorded using a Panalytical Empyrean diffractometer (Malvern Panalytical, Malvern, UK) equipped with a Cu target, giving Cu K $\alpha$ 1/2 radiation. Data were recorded in reflection, Bragg–Brentano geometry from samples in silicon plates. The powder diffraction patterns were analysed using the GSAS-II software [36], with Pawley or Rietveld fits performed using published crystal structures of NaTaO<sub>3</sub> as a starting point to refine lattice parameters. Powder X-ray thermodiffraction was performed using a Bruker D8 instrument (Bruker AXS Ltd., Coventry, UK) with Cu K $\alpha$ 1/2 radiation and fitted with an Anton Paar XRK 900 chamber (Anton Paar GmbH, Graz, Austria) and a V $\dot{A}$ NTEC solid-state detector (Bruker AXS Ltd, Coventry, UK); this allowed heating of a sample from room temperature to 900 °C and XRD patterns were recorded at intervals of 50 °C. Before each data collection, the temperature was allowed to equilibrate for 5 min.

Scanning electron microscopy was performed using a ZEISS SUPRA 55-VP FEGSEM scanning electron microscope (Oberkochen, Germany) using a field emission gun with an accelerating voltage between 5 and 20 kV and fitted with an Oxford Instruments (Abingdon, UK) energy-dispersive X-ray spectroscopy (EDS) spectrometer that allows elemental composition analysis

Scanning transmission electron microscopy (STEM) was performed using a JEOL ARM200F double aberration corrected instrument (Welwyn Garden City, UK) operating at 200 kV. Specimens were dispersed by ultrasound in ethanol and dropped onto 3 mm lacey carbon grids supplied by Agar Scientific (Stansted, UK). Annular dark field STEM (ADF-STEM) images were obtained using a JEOL annular field detector at a probe current of ~23 pA with a convergence semi-angle of ~25 mrad. Energy-dispersive X-ray spectroscopy (EDS) measurements were carried out with an Oxford Instruments X-MaxN100TLE windowless silicon drift detector (Abingdon, UK) to determine the elemental composition and distribution. The program cITEM [37] was utilised to produce simulations of ADF-STEM images based on the crystal model oriented at (010) zone axis over an area of 1.5 nm by 2.6 nm. Inelastic phonon scattering was applied using the frozen

phonon approximation method via an iterative approach to resemble molecular deviation from its equilibrium position under the electron probe at room temperature. The following thermal parameters ( $\langle u^2 \rangle$ ) were used during simulation: 0.0166 Å<sup>2</sup> Na, 0.0048 Å<sup>2</sup> Ta, and 0.0080 Å<sup>2</sup> for O [38].

X-ray absorption near-edge spectroscopy (XANES) spectra at the iridium L<sub>III</sub>-edge were recorded using Beamline B18 of the Diamond Light Source, Harwell, UK [39]. Data were collected in transmission mode from samples diluted with appropriate amounts of polyethylene powder (~20% sample by mass) and pressed into self-supporting discs around 1 mm thick. Incident energies were selected using a water-cooled, fixed-exit, double-crystal monochromator with Si(111) crystals. The beam was focused horizontally and vertically using a double toroidal mirror, coated with Pt, 25 m from the source, while a pair of smaller plane mirrors were used for harmonic rejection. The raw data were normalised using the software ATHENA (version 0.9.26) [40] to produce XANES spectra.

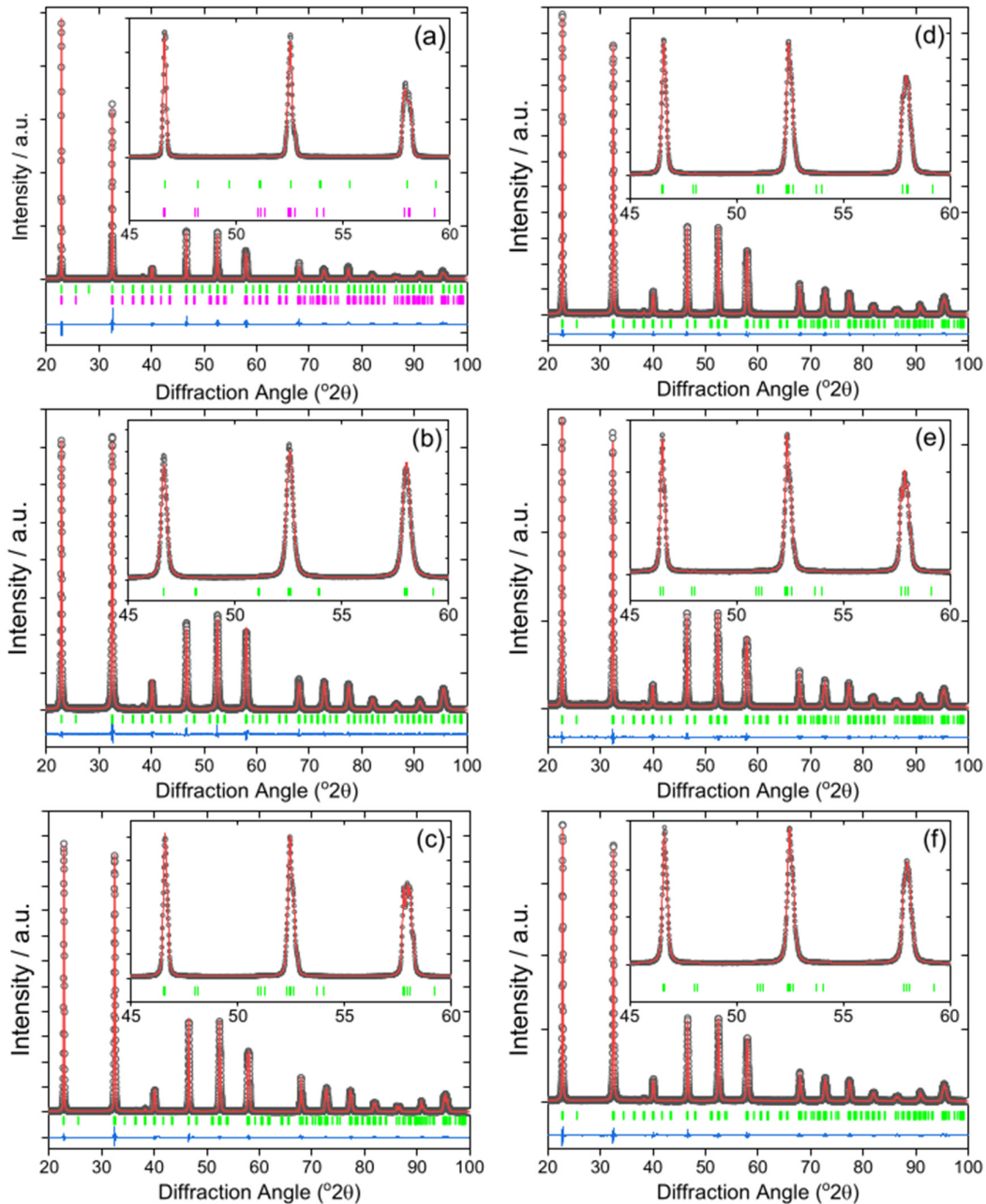
Diffuse reflectance spectroscopy was performed on powder samples using a Shimadzu UV-2600i UV-Vis spectrophotometer (Milton Keynes, UK). A barium sulfate standard was used as a baseline for the measurements.

The photocatalytic hydrogen production was performed in a Pyrex glass vessel with a top quartz window for vertical illumination in a closed-gas circulation system. In a typical run, 45 mg of catalyst was suspended in 20 vol% methanol solution in water. Then, 1.0 wt.% of Pt was loaded on the photocatalyst particles via photodeposition as a cocatalyst, to provide H<sub>2</sub> evolution sites. The glass reactor vessel was then sealed and repeatedly vacuumed by a rotary pump and purged with argon gas to remove the residual air. Subsequently, the reactor was irradiated with an 800 W Xe-Hg lamp (Newport, RI, USA) from the top, with full-spectrum intensity of 200 mW cm<sup>-2</sup>. Experiments were also performed with visible light (420 nm cut-off filter) with intensity of 100 mW cm<sup>-2</sup>. The infrared component in the radiation was removed by a circulating water filter. The temperature in the reactor was maintained at 25 °C by external water circulation. The amount of generated H<sub>2</sub> gas was quantitatively analysed every 2 h by a gas chromatograph (Shimadzu GC-2014; Molecular sieve 5A, TCD detector, Ar carrier gas) (Shimadzu, Duisburg, Germany).

### 3. Results

The iridium-containing samples are all produced as green powders, in contrast to the white parent NaTaO<sub>3</sub>. The powder XRD pattern of the unsubstituted NaTaO<sub>3</sub> material was initially fitted using the orthorhombic space group, *Pbnm*, but a closer examination of the pattern revealed some mismatched peak intensities, which could be remedied by inclusion of a second *Cmcm* polymorph. A two-phase Rietveld analysis with atom coordinates and temperature factors fixed at the values reported in the literature [41], gave a satisfactory fit to the data, Figure 1a. The refined lattice parameters are in agreement with the literature values, Table 1, and the mixed-phase nature of NaTaO<sub>3</sub> has been previously seen, with samples prepared by solid-state synthesis showing ~45% of the *Cmcm* polymorph [38]. The smaller amount of the second polymorph that we observe (24.9%) would be consistent with the different synthesis route that we have used, but it is noteworthy that the hydrothermal method yields a proportion of the *Cmcm* polymorph, that has been defined as a high-temperature phase. The powder XRD patterns of the iridium substituted sodium tantalate materials can all be fitted using the single *Pbnm* polymorph, Figure 1b–f. The variation of lattice parameters with intended Ir content, Table 1 and Figure 2, provides evidence for the inclusion of Ir into the perovskite structure, in particular since all materials with the highest Ir content have larger orthorhombic *c* axes and corresponding larger unit cell volumes. It can be seen that the material with the smallest intended Ir amount has unit cell parameters rather similar to the parent NaTaO<sub>3</sub>. The ionic radius of both Ir<sup>4+</sup> (0.625 Å) and Ir<sup>5+</sup> (0.570 Å) in octahedral coordination are similar to Ta<sup>5+</sup> (0.640 Å) [42]. Given that it is most likely that the tantalum is replaced in the perovskite, we can propose that a smaller Ir content may be associated with the higher

oxidation state, while addition of larger quantities results in inclusion of more Ir<sup>4+</sup>, with associated charge-balancing oxide-ion vacancies, and hence modification of the lattice parameters. The iridium oxidation state will be discussed further below in the light of spectroscopic evidence. If larger amounts of iridium were added to the synthesis, then no further inclusion of Ir into the perovskite structure was observed and instead poorly crystalline IrO<sub>2</sub> was formed as a byproduct.

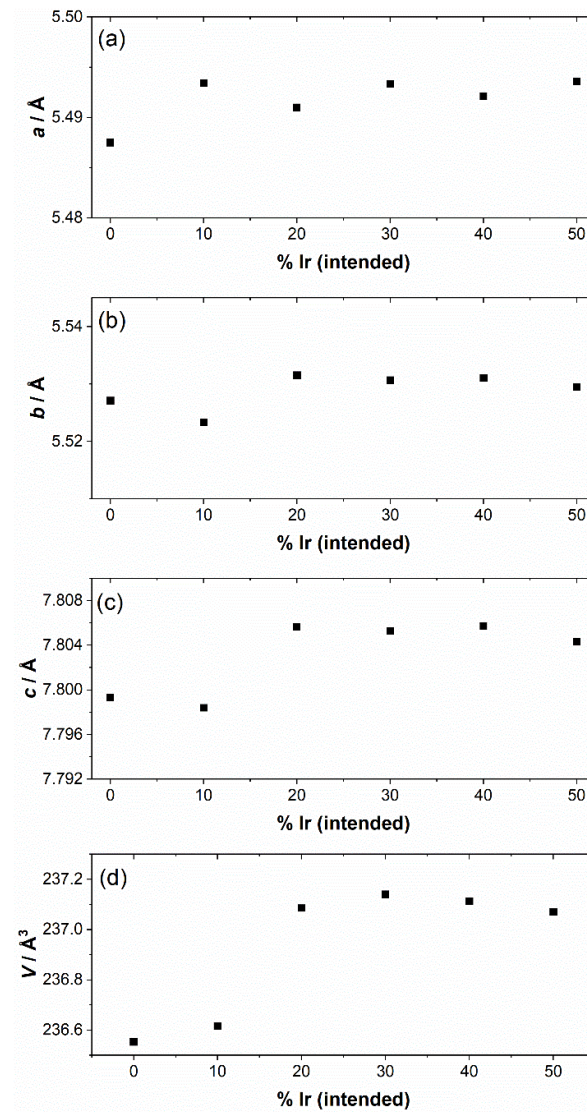


**Figure 1.** Fitted powder XRD patterns ( $\lambda = 1.5418 \text{ \AA}$ ) of Ir-NaTaO<sub>3</sub> prepared by hydrothermal synthesis with intended Ir content of (a) 0% ( $R_w = 9.787$ ), (b) 10% ( $R_w = 6.070$ ), (c) 20% ( $R_w = 4.969$ ), (d) 30% ( $R_w = 4.767$ ), (e) 40% ( $R_w = 6.089$ ), (f) 50% ( $R_w = 6.767$ ). The data are the black circles, the red line is the fitted pattern, the blue line is the difference curve, and the green tick marks are the positions of allowed Bragg reflections (space group, *Pbnm*). In (a), the second set of pink tick marks are due to the minor *Cmcm* phase, where a Rietveld fit was used. (b–f) are Pawley fits.

**Table 1.** Refined lattice parameters of substituted sodium tantalates from analysis of powder XRD data. The intended level of Ir substitution is indicated.

Material	Lattice Parameters		
	$a/\text{\AA}$	$b/\text{\AA}$	$c/\text{\AA}$
NaTaO <sub>3</sub> [41]	5.48109(9)	5.52351(9)	7.79483(12)
NaTaO <sub>3</sub> <sup>a</sup>	5.48750(5)	5.52711(6)	7.7993(1)
NaTaO <sub>3</sub> -10% Ir	5.4934(1)	5.5233(1)	7.7984(2)
NaTaO <sub>3</sub> -20% Ir	5.49099(4)	5.53154(5)	7.8056(6)
NaTaO <sub>3</sub> -30% Ir	5.49335(6)	5.53067(9)	7.8053(1)
NaTaO <sub>3</sub> -40% Ir	5.49212(8)	5.53101(9)	7.8057(1)
NaTaO <sub>3</sub> -50% Ir	5.4936(1)	5.5295(1)	7.8043(1)

<sup>a</sup>: The major (75.1%) *Pbmm* phase is shown, the second *Cmcm* phase has lattice parameters  $a = 7.795(2)$  Å,  $b = 7.789(3)$  Å,  $c = 7.791(5)$  Å (cf. literature values [38],  $a = 7.77927(8)$  Å,  $b = 7.7815(2)$  Å,  $c = 7.7899(1)$  Å).

**Figure 2.** Variation of lattice parameters of Ir-NaTaO<sub>3</sub> materials with intended composition. (a)  $a$ , (b)  $b$ , (c)  $c$ , and (d) unit cell volume. The error bars are smaller than the data points.

The iridium-substituted sodium tantalates are formed as nanocubes with edges in the range of up to a few hundreds of nanometres, and typically ~100 nm, as seen by STEM, Figure 3. Although the cubes are not monodisperse in size, they have high crystallinity, as evidenced by high-resolution atomic-scale imaging, Figure 3g. EDS maps measured in STEM show an even dispersion of iridium in the substituted materials, with no evidence of clustering of iridium, nor any distinct particles of separate iridium-rich material, such as iridium oxide, or iridium metal, Figure 4. The cube-shaped particles are similar to hydrothermally synthesised sodium tantalate reported in literature [43–45], including those substituted with  $\text{Bi}^{3+}$  [46] and  $\text{Cu}^{2+}$  [47].

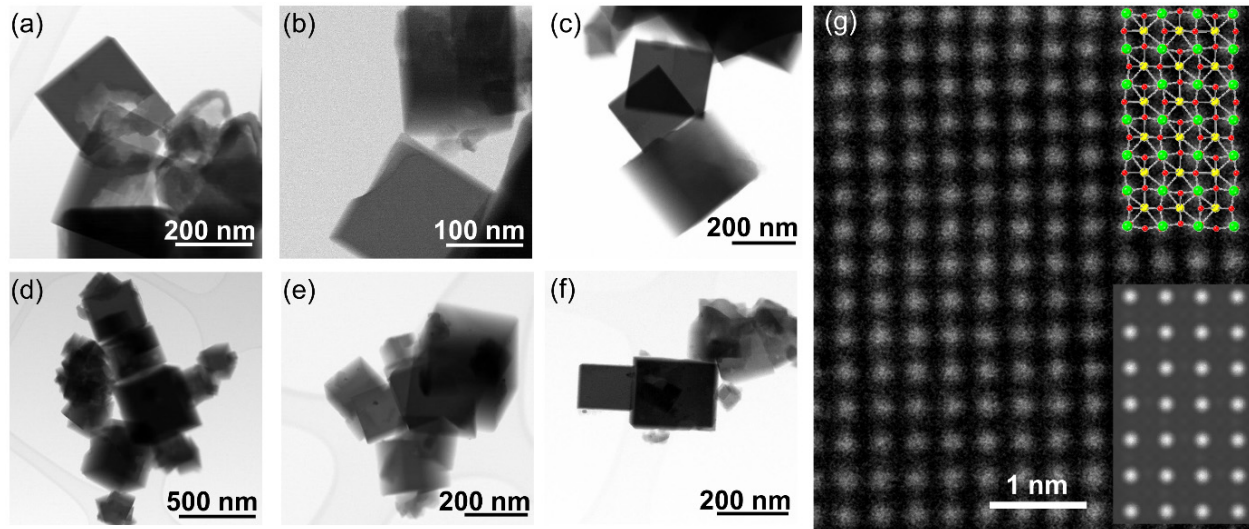


**Figure 3.** TEM images of Ir-substituted  $\text{NaTaO}_3$  materials with intended Ir content of (a) 0%, (b) 10%, (c) 20%, (d) 30%, (e) 40% and (f) 50%. See Supporting Information for further images of the specimens. (g) shows a high-resolution TEM image of the 40% Ir material, with the simulated image (lower inset) and the corresponding crystal structure (upper inset, where green atoms are Ta(Ir), yellow are sodium, and red are oxygen).

Quantification of the EDS performed using scanning electron microscopy reveals that the iridium content of the materials is somewhat lower than the amounts used in the reactions used to prepare them, Table 2. This is consistent with the strong colour of the filtrate during washing of the samples, which suggests not all the precious metal was incorporated into the final material. Nevertheless, the amount of iridium does increase proportionally with increasing amount used in synthesis.

**Table 2.** EDXA of Ir-substituted  $\text{NaTaO}_3$  materials performed using scanning electron microscopy.

Intended Ir Substitution	Tantalum/%	EDS Results	
		Iridium/%	Determined Formula
10%	97.6	2.4	$\text{NaTa}_{0.98}\text{Ir}_{0.02}\text{O}_3$
20%	95.3	4.7	$\text{NaTa}_{0.95}\text{Ir}_{0.05}\text{O}_3$
30%	91.6	8.4	$\text{NaTa}_{0.92}\text{Ir}_{0.08}\text{O}_3$
40%	87.8	12.2	$\text{NaTa}_{0.88}\text{Ir}_{0.12}\text{O}_3$
50%	85.1	14.9	$\text{NaTa}_{0.85}\text{Ir}_{0.15}\text{O}_3$

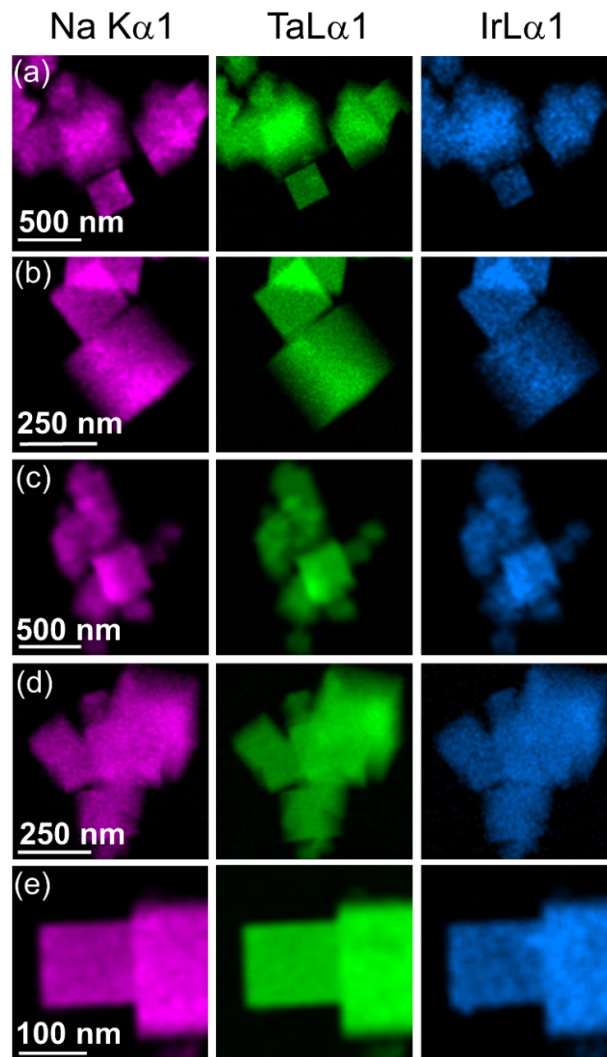


**Figure 4.** EDS maps performed using TEM of Ir-substituted  $\text{NaTaO}_3$  materials with intended Ir content of (a) 10%, (b) 20%, (c) 30%, (d) 40%, and (e) 50%.

Three representative samples were studied in more detail to understand the chemical state of iridium in the samples. XANES spectra recorded at the Ir  $L_{III}$ -edge, Figure 5, were used to determine the average oxidation state of iridium by comparison to reference materials. Here, the position of the white line was used as a measure of edge shift, as in our previous work [48], and the materials  $\text{IrCl}_3$ ,  $\text{IrO}_2$ , and  $\text{BaNa}_{0.5}\text{Ir}_{0.5}\text{O}_{3-x}$  ( $x = 0.525$ ) were used as calibrants for oxidation states +3, +4, and +4.9, respectively. This shows that the iridium in the materials with higher levels of Ir has an oxidation state of close to +4, as in  $\text{IrO}_2$ , Figure 6. The sample with the lowest iridium content appears to have a higher average Ir oxidation state, but still lower than +5. The chemistry of  $\text{Ir}^{4+}$  and  $\text{Ir}^{5+}$  in oxides is almost exclusively associated with octahedral coordination [49] and so it is anticipated that iridium occupies the B-site of the perovskite structure.



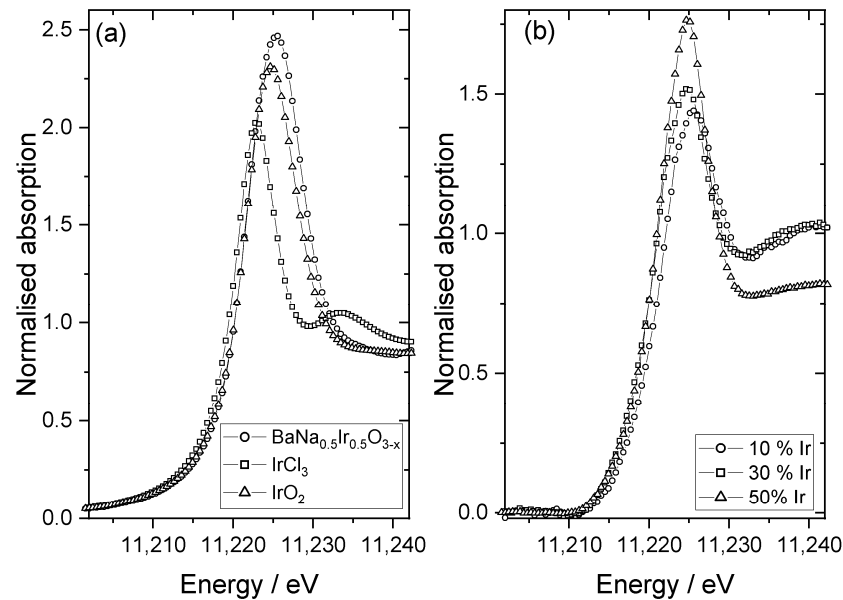


**Figure 5.** Ir  $L_{III}$ -edge XANES spectra: (a) reference materials for oxidation state calibration and (b) Ir-substituted  $\text{NaTaO}_3$  materials labelled according to the proportion of Ir added in synthesis.

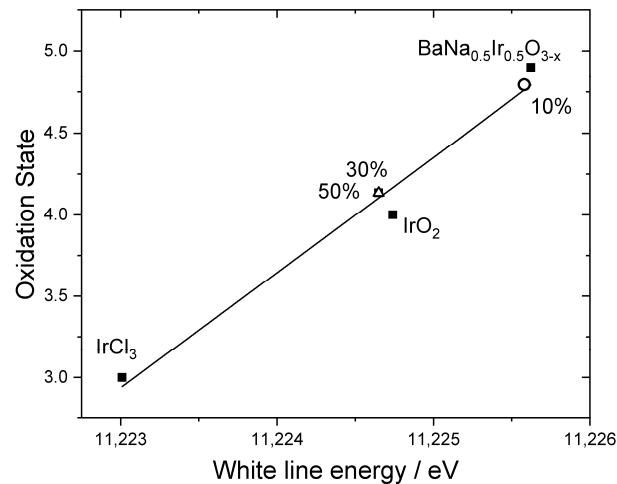


**Figure 6.** Oxidation states of Ir-substituted  $\text{NaTaO}_3$  materials labelled according to the proportion of Ir added in synthesis, plotted with reference materials. The line is the linear regression fit to the points from the reference materials.

The results of the XANES analysis are consistent with the results from powder XRD, as described above. The sample with the smallest amount of iridium contains a significant proportion of  $\text{Ir}^{5+}$ , which would be consistent with the small changes in lattice parameter, but the materials with greater Ir content contain  $\text{Ir}^{4+}$ , which is larger in ionic radius and would require charge-balancing oxide-ion vacancies, and hence rather different lattice parameters. The reason for this difference is not apparent from the data we have measured, and it may be the case that a greater surface accumulation of Ir at the higher amounts used leads to a change in average oxidation state of iridium, or that the redox chemistry in solution leads to only small amounts of  $\text{Ir}^{5+}$  that are available for inclusion in the perovskite structure.

Figure 7 shows diffuse-reflectance UV-vis spectra measured from the same three samples, along with the spectrum of  $\text{NaTaO}_3$  for comparison. The parent perovskite  $\text{NaTaO}_3$  shows a spectrum very similar to that reported from the literature [50], and a

Tauc plot analysis gives a direct band gap of 4.0 eV, as expected. The iridium-containing materials show significant absorption in the visible part of the spectrum, which illustrates the green colour of the powdered samples, with strong absorptions in the 450 nm and 700 nm regions. Interestingly, the sample with smallest iridium content shows different absorption maxima to the samples with the higher iridium content, suggesting a different electronic state for the iridium cations in the solid. This is entirely consistent with the XANES and powder XRD analysis presented above.

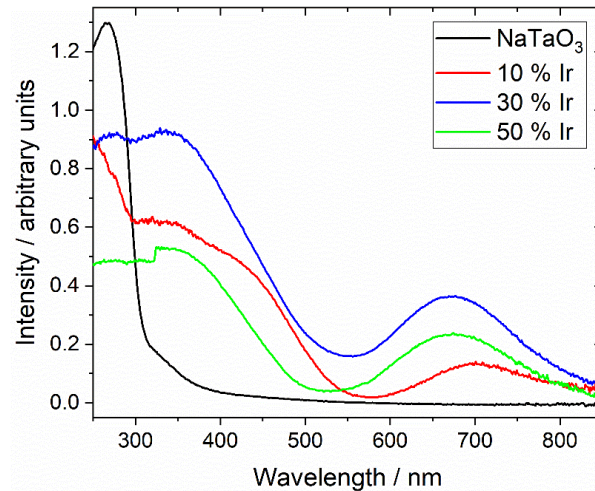


**Figure 7.** Diffuse-reflectance UV-vis spectra of Ir-substituted  $\text{NaTaO}_3$  materials labelled according to the proportion of Ir added in synthesis.

We examined the materials use in photocatalysis by studying hydrogen generation from water using the material with highest iridium content. To optimise the activity, the powders were heated in air at 500 °C to remove any surface-bound water and minimise any possible hydroxyl defects that may be anticipated in hydrothermally produced oxide perovskites [51–53]. To verify that this did not result in phase separation, X-ray powder thermodiffraction was carried out with heating from room temperature to 900 °C, Figure 8. This shows that the perovskite structure remains unchanged until above 600 °C and only then are the strongest Bragg peaks of face-centred cubic iridium metal [54] observed.

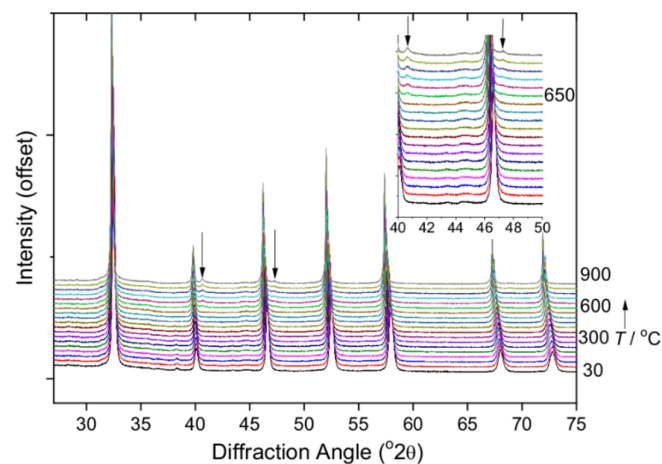


**Figure 8.** Variable temperature XRD on heating in air showing the stability of  $\text{Na}(\text{Ta},\text{Ir})\text{O}_3$  until above 600 °C when iridium metal is seen, with its two strongest Bragg peaks, (111) and (200), indicated by the arrows.

Photocatalysis results reveal that the parent  $\text{NaTaO}_3$  when loaded with 1 wt.% Pt shows a low activity in full-spectrum irradiation, but no detectable activity under visible light towards hydrogen evolution in aqueous methanol, Figure 9. In contrast, the full-spectrum irradiation of  $\text{Na}(\text{Ta},\text{Ir})\text{O}_3$  yields approximately 15 times the yield of hydrogen, and, notably, under visible light shows yields of hydrogen comparable to the unsubstituted material in UV + visible light. These preliminary results demonstrate the effectiveness of iridium substitution in tuning optical properties of  $\text{NaTaO}_3$  to provide visible light activity. We note that the catalytic production of hydrogen is not linear, but this has been reported previously for Bi-containing  $\text{NaTaO}_3$  studied under the same conditions [55]. The cause of this is not known at present, but may be related to a change of the catalyst surface with time, such as restructuring of surface defects.

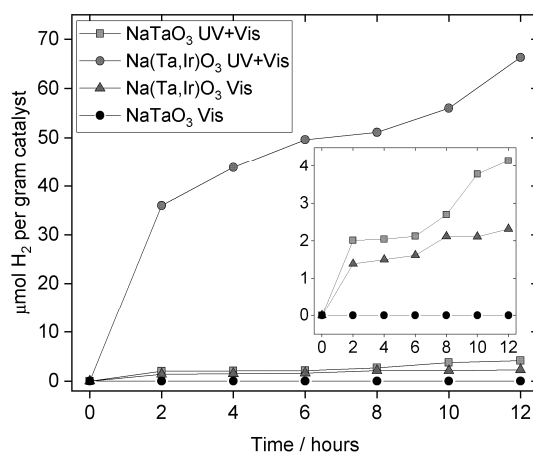


**Figure 9.** Photocatalytic hydrogen evolution observed from  $\text{NaTaO}_3$  and Ir-substituted sample.

#### 4. Discussion

The observation of iridium in oxidation states between +4 and +5 in the perovskite structure is consistent with other iridium oxides that contain octahedrally coordinated Ir and that have been prepared under similar hydrothermal conditions in alkali solutions in the presence of peroxide as oxidant [35,48]. It is noteworthy that for the material with the lowest iridium concentration a higher oxidation state is observed spectroscopically, while increasing Ir concentration lowers the average Ir oxidation state (corroborated indirectly by powder XRD). Interestingly, for other iridium-substituted perovskites reported in the literature via other synthesis methods, different oxidation states of Ir may be found. For example, Cali et al. observed  $\text{Ir}^{3+}$  using X-ray photoelectron spectroscopy in 5 mol% Ir-substituted  $\text{SrTiO}_3$  that had been prepared by solid-state synthesis at 1340 °C [31]. On the other hand, Kawasaki et al. found  $\text{Ir}^{4+}$  in samples of Ir-substituted  $\text{SrTiO}_3$  prepared by solid-state synthesis at 1100 °C [32]. While the valence states of the host perovskite material might influence the Ir oxidation state, the synthesis method is likely to play an important role, and hence the hydrothermal method offers an alternative approach to solid-state synthesis that might allow a more tunable synthesis of Ir-containing perovskites.

The presence of  $\text{Ir}^{4+}$  in  $\text{NaTaO}_3$  means that charge-balancing defects must be necessary. In other precious-metal-doped perovskites, surface oxide defects have been inferred, for example, in Ir- $\text{SrTiO}_3$  [32]. In the case of  $\text{NaTaO}_3$  prepared by hydrothermal synthesis, inclusion of  $\text{Bi}^{3+}$  was accompanied by oxide defects, based on evidence from photoluminescence spectra [46]. It is also a possibility that the hydrothermal route allows charge-balance by inclusion of hydroxide ions in place of oxide: these have been detected in other perovskites prepared by this method, such as  $\text{Na}_{0.5}\text{Bi}_{0.5}\text{TiO}_3$  [51,53] and  $\text{KNbO}_3$  [52]. Defects such as anion vacancies may be in part responsible for the enhanced light absorption and photocatalytic activity of the substituted materials [56]. Further in-depth

experimental work is needed to explore the role of defects and how these are modified in the presence of the co-catalyst, and with heat treatment. Methods such X-ray photoelectron spectroscopy would be useful to example the nature of oxide defects, such as lattice vacancies [57].

The materials we have prepared show stability on heating in air to only 600 °C, which demonstrates how it would be impossible to prepare the same samples by conventional solid-state synthesis, or even coprecipitation methods that require an annealing step. It is interesting to note that Rh<sup>3+</sup>-containing BaTiO<sub>3</sub> prepared by an oxalate-aided coprecipitation route showed extrusion of rhodium metal when heated above its synthesis temperature [30]. This illustrates the tendency for the precious metals to be reduced, but also how this may be aided by embedding in a host lattice by replacement of a cation of higher charge.

Our photocatalysis results show the beneficial effect of Ir-inclusion in NaTaO<sub>3</sub> with greater than ten-fold enhancement of activity towards hydrogen evolution in UV+visible radiation, a significant part of which can be ascribed to visible light absorption. The results obtained are a similar order of magnitude to those produced from Bi<sup>3+</sup>-NaTaO<sub>3</sub>, studied using the same experimental protocol [55], although they do not reach such a high hydrogen yield. However, there is scope for further optimisation, as the previous work showed how Pt loading and substitution level of the perovskite should be adjusted to improve yield, and that the surface area of the materials should be controlled for maximum catalytic efficiency. In optimising photocatalytic properties for hydrogen evolution of Ir-SrTiO<sub>3</sub> the oxidation state of Ir is important [32], but also loading with surface Ir metal can optimise properties [58]. Hence, our work provides a convenient synthesis method that may allow further tuning of properties of materials for visible-light photocatalysis.

## 5. Conclusions

We have presented a hydrothermal synthesis route to introduce iridium into a prototypical perovskite structure NaTaO<sub>3</sub> that uses mild reaction conditions in a single-step process. A comprehensive set of characterisation data shows that the iridium replaces tantalum to give small adjustments in lattice parameters. For the samples that contain the most iridium, the substituent is present in the +4 oxidation state, which implies the presence of defects for charge balance, but this is in line with other perovskites that contain precious-metal substituents, and for other oxides that have been prepared by hydrothermal chemistry. Our preliminary photocatalysis results show promising properties for visible-light generation of hydrogen from water, but beyond this the materials may prove useful for other applications in heterogeneous catalysis, either as prepared, or upon reduction to extrude the iridium as supported nanocrystals. Finally, we note that the redox chemistry taking place during synthesis as the Ir<sup>3+</sup> precursor is oxidised is likely to be complex, and this is where the origin of the substitutional chemistry occurs. Further work is needed to understand the mechanisms of hydrothermal crystallisation of oxides, and the evolution of the solution chemistry as a solid is formed is largely unexplored at present.

**Author Contributions:** Conceptualization, R.I.W.; materials synthesis, D.L.B. and C.D.V.; data collection and analysis; D.L.B., J.A.C. and R.J.K.; writing—original draft preparation, R.I.W.; writing—reviewing and editing, D.L.B., J.A.C., R.I.W.; funding acquisition, R.I.W. All authors have read and agreed to the published version of the manuscript.

**Funding:** The research work was supported by EPSRC (University of Warwick Doctoral Training account EP/K503204/1).

**Data Availability Statement:** The research data underpinning this article can be accessed at: <http://wrap.warwick.ac.uk/15386> (accessed on 9 June 2021).

**Acknowledgments:** We thank the EPSRC for funding a PhD studentship to DLB in collaboration with Johnson Matthey, and the University of Warwick Undergraduate Research Support Scheme for provision of a scholarship to CDV. We are grateful to Chen Zhong and Qiuling Tay at NTU Singapore for measurement of photocatalysis, Diamond Light Source for provision of beamtime (SP8708), Tom Chamberlain for measuring UV-Vis spectra, and Giannantonio Cibir for assistance with measuring the XANES spectra. Some of the equipment used in this work was provided by the University of Warwick's Research Technology Platforms.

**Conflicts of Interest:** The authors declare no conflict of interest.

## References

1. Walton, R.I. Perovskite Oxides Prepared by Hydrothermal and Solvothermal Synthesis: A Review of Crystallisation, Chemistry, and Compositions. *Chem. Eur. J.* **2020**, *26*, 9041–9069.
2. Sato, Y.; Aoki, M.; Teranishi, R.; Kaneko, K.; Takesada, M.; Moriwake, H.; Takashima, H.; Hakuta, Y. Atomic-Scale Observation of Titanium-Ion Shifts in Barium Titanate Nanoparticles: Implications for Ferroelectric Applications. *ACS Appl. Nano Mater.* **2019**, *2*, 5761–5768.
3. Morita, T. Piezoelectric Materials Synthesized by the Hydrothermal Method and Their Applications. *Materials* **2010**, *3*, 5236–5245.
4. Sardar, K.; Lees, M.R.; Kashtiban, R.J.; Sloan, J.; Walton, R.I. Direct Hydrothermal Synthesis and Physical Properties of Rare-Earth and Yttrium Orthochromite Perovskites. *Chem. Mat.* **2011**, *23*, 48–56.
5. Diodati, S.; Walton, R.I.; Mascotto, S.; Gross, S. Low-Temperature wet chemistry synthetic approaches towards ferrites. *Inorg. Chem. Front.* **2020**, *7*, 3282–3314.
6. Eckert, J.O.; HungHouston, C.C.; Gersten, B.L.; Lencka, M.M.; Riman, R.E. Kinetics and mechanisms of hydrothermal synthesis of barium titanate. *J. Amer. Ceram. Soc.* **1996**, *79*, 2929–2939.
7. Sōmiya, S.; Roy, R. Hydrothermal synthesis of fine oxide powders. *Bull. Mater. Sci.* **2000**, *23*, 453–460.
8. Riman, R.E.; Suchanek, W.L.; Lencka, M.M. Hydrothermal crystallization of ceramics. *Ann. Chim. Sci. Mater.* **2002**, *27*, 15–36.
9. Walton, R.I. Subcritical solvothermal synthesis of condensed inorganic materials. *Chem. Soc. Rev.* **2002**, *31*, 230–238.
10. Komarneni, S. Nanophase materials by hydrothermal, microwave-hydrothermal and microwave-solvothermal methods. *Curr. Sci.* **2003**, *85*, 1730–1734.
11. Yoshimura, M.; Byrappa, K. Hydrothermal processing of materials: Past, present and future. *J. Mater. Sci.* **2008**, *43*, 2085–2103.
12. Kumada, N. Preparation and crystal structure of new inorganic compounds by hydrothermal reaction. *J. Ceram. Soc. Jap.* **2013**, *121*, 135–141.
13. Shi, J.; Li, J.; Huang, X.; Tan, Y. Synthesis and enhanced photocatalytic activity of regularly shaped Cu<sub>2</sub>O nanowire polyhedra. *Nano Res.* **2011**, *4*, 448–459.
14. Deng, S.; Tjoa, V.; Fan, H.M.; Tan, H.R.; Sayle, D.C.; Olivo, M.; Mhaisalkar, S.; Wei, J.; Sow, C.H. Reduced Graphene Oxide Conjugated Cu<sub>2</sub>O Nanowire Mesocrystals for High-Performance NO<sub>2</sub> Gas Sensor. *J. Am. Chem. Soc.* **2012**, *134*, 4905–4917.
15. Ding, Y.; Guo, X.; Du, B.; Hu, X.; Yang, X.; He, Y.; Zhou, Y.; Zang, Z. Low-operating temperature ammonia sensor based on Cu<sub>2</sub>O nanoparticles decorated with p-type MoS<sub>2</sub> nanosheets. *J. Mater. Chem. C* **2021**, *9*, 4838–4846.
16. Chen, S.; Zhu, J.W.; Wu, X.D.; Han, Q.F.; Wang, X. Graphene Oxide-MnO<sub>2</sub> Nanocomposites for Supercapacitors. *ACS Nano* **2010**, *4*, 2822–2830.
17. Modeshia, D.R.; Darton, R.J.; Ashbrook, S.E.; Walton, R.I. Control of polymorphism in NaNbO<sub>3</sub> by hydrothermal synthesis. *Chem. Commun.* **2009**, 68–70.
18. Skjaervø, S.L.; Sommer, S.; Norby, P.; Bojesen, E.D.; Grande, T.; Iversen, B.B.; Einarsrud, M.A. Formation mechanism and growth of MNbO<sub>3</sub>, M = K, Na by in situ X-ray diffraction. *J. Amer. Ceram. Soc.* **2017**, *100*, 3835–3842.
19. Skjaervø, S.L.; Wells, K.H.; Sommer, S.; Vu, T.D.; Tolchard, J.R.; van Beek, W.; Grande, T.; Iversen, B.B.; Einarsrud, M.A. Rationalization of Hydrothermal Synthesis of NaNbO<sub>3</sub> by Rapid in Situ Time-Resolved Synchrotron X-ray Diffraction. *Cryst. Growth Des.* **2018**, *18*, 770–774.
20. Song, H.W.; Ma, W.H. Hydrothermal synthesis of submicron NaNbO<sub>3</sub> powders. *Ceram. Int.* **2011**, *37*, 877–882.
21. Kumada, N.; Dong, Q.; Yonesaki, Y.; Takei, T.; Kinomura, N. Hydrothermal synthesis of NaNbO<sub>3</sub>-morphology change by starting compounds. *J. Ceram. Soc. Jap.* **2011**, *119*, 483–485.
22. Shi, G.D.; Wang, J.H.; Wang, H.L.; Wu, Z.J.; Wu, H.P. Hydrothermal synthesis of morphology-controlled KNbO<sub>3</sub>, NaNbO<sub>3</sub>, and (K,Na)NbO<sub>3</sub> powders. *Ceram. Int.* **2017**, *43*, 7222–7230.
23. Nakashima, K.; Tushima, Y.; Kobayashi, Y.; Kakihana, M. Effects of raw materials on NaNbO<sub>3</sub> nanocube synthesis via the solvothermal method. *J. As. Ceram. Soc.* **2019**, *7*, 36–41.
24. Kanie, K.; Numamoto, Y.; Tsukamoto, S.; Takahashi, H.; Mizutani, H.; Terabe, A.; Nakaya, M.; Tani, J.; Muramatsu, A. Hydrothermal Synthesis of Sodium and Potassium Niobates Fine Particles and Their Application to Lead-Free Piezoelectric Material. *Mater. Trans.* **2011**, *52*, 2119–2125.
25. Pan, H.; Zhu, G.S.; Chao, X.L.; Wei, L.L.; Yang, Z.P. Properties of NaNbO<sub>3</sub> powders and ceramics prepared by hydrothermal reaction. *Mater. Chem. Phys.* **2011**, *126*, 183–187.

26. Fukada, M.; Shibata, K.; Imai, T.; Yamazoe, S.; Hosokawa, S.; Wada, T. Fabrication of lead-free piezoelectric NaNbO<sub>3</sub> ceramics at low temperature using NaNbO<sub>3</sub> nanoparticles synthesized by solvothermal method. *J. Ceram. Soc. Jap.* **2013**, *121*, 116–119.
27. Shi, H.F.; Li, X.K.; Wang, D.F.; Yuan, Y.P.; Zou, Z.G.; Ye, J.H. NaNbO<sub>3</sub> Nanostructures: Facile Synthesis, Characterization, and Their Photocatalytic Properties. *Catal. Lett.* **2009**, *132*, 205–212.
28. Kanhere, P.; Chen, Z. A Review on Visible Light Active Perovskite-Based Photocatalysts. *Molecules* **2014**, *19*, 19995–20022.
29. Polat, O.; Durmus, Z.; Coskun, F.M.; Coskun, M.; Turut, A. Engineering the band gap of LaCrO<sub>3</sub> doping with transition metals (Co, Pd, and Ir). *J. Mater. Sci.* **2018**, *53*, 3544–3556.
30. Lontio Fomekong, R.; You, S.; Enrichi, F.; Vomiero, A.; Saruhan, B. Impact of Oxalate Ligand in Co-Precipitation Route on Morphological Properties and Phase Constitution of Undoped and Rh-Doped BaTiO<sub>3</sub> Nanoparticles. *Nanomaterials* **2019**, *9*, 1697.
31. Cali, E.; Kerherve, G.; Naufal, F.; Kousi, K.; Neagu, D.; Papaioannou, E.I.; Thomas, M.P.; Guiton, B.S.; Metcalfe, I.S.; Irvine, J.T.S.; et al. Exsolution of Catalytically Active Iridium Nanoparticles from Strontium Titanate. *ACS Appl. Mater. Interfaces* **2020**, *12*, 37444–37453.
32. Kawasaki, S.; Takahashi, R.; Akagi, K.; Yoshinobu, J.; Komori, F.; Horiba, K.; Kumigashira, H.; Iwashina, K.; Kudo, A.; Lippmaa, M. Electronic Structure and Photoelectrochemical Properties of an Ir-Doped SrTiO<sub>3</sub> Photocatalyst. *J. Phys. Chem. C* **2014**, *118*, 20222–20228.
33. Iwase, A.; Saito, K.; Kudo, A. Sensitization of NaMO<sub>3</sub> (M: Nb and Ta) Photocatalysts with Wide Band Gaps to Visible Light by Ir Doping. *Bull. Chem. Soc. Jap.* **2009**, *82*, 514–518.
34. Kudo, A.; Yoshino, S.; Tsuchiya, T.; Udagawa, Y.; Takahashi, Y.; Yamaguchi, M.; Ogasawara, I.; Matsumoto, H.; Iwase, A. Z-scheme photocatalyst systems employing Rh- and Ir-doped metal oxide materials for water splitting under visible light irradiation. *Farad. Disc.* **2019**, *215*, 313–328.
35. Sardar, K.; Fisher, J.; Thompsett, D.; Lees, M.R.; Clarkson, G.J.; Sloan, J.; Kashtiban, R.J.; Walton, R.I. Structural variety in iridate oxides and hydroxides from hydrothermal synthesis. *Chem. Sci.* **2011**, *2*, 1573–1578.
36. Toby, B.H.; von Dreele, R.B. GSAS-II: The genesis of a modern open-source all purpose crystallography software package. *J. Appl. Cryst.* **2013**, *46*, 544–549.
37. Peters, J.J.P. cITEM. Available online: <https://jjppeters.github.io/cITEM/> (accessed on 19 March 2021).
38. Knight, K.S.; Kennedy, B.J. Phase coexistence in NaTaO<sub>3</sub> at room temperature; a high resolution neutron powder diffraction study. *Solid State Sci.* **2015**, *43*, 15–21.
39. Dent, A.J.; Cibir, G.; Ramos, S.; Smith, A.D.; Scott, S.M.; Varandas, L.; Pearson, M.R.; Krumpa, N.A.; Jones, C.P.; Robbins, P.E. B18: A core XAS spectroscopy beamline for Diamond. *J. Phys. Conf. Ser.* **2009**, *190*, 012039.
40. Ravel, B.; Newville, M. ATHENA, ARTEMIS, HEPHAESTUS: Data analysis for X-ray absorption spectroscopy using IFEFFIT. *J. Synchrotron Rad.* **2005**, *12*, 537–541.
41. Mitchell, R.H.; Liferovich, R.P. A structural study of the perovskite series Ca<sub>1-x</sub>Na<sub>x</sub>Ti<sub>1-x</sub>Ta<sub>x</sub>O<sub>3</sub>. *J. Solid State Chem.* **2004**, *177*, 4420–4427.
42. Shannon, R. Revised effective ionic radii and systematic studies of interatomic distances in halides and chalcogenides. *Acta Crystallogr. Sect. A* **1976**, *32*, 751–767.
43. Gao, Y.; Su, Y.G.; Meng, Y.; Wang, S.W.; Jia, Q.Y.; Wang, X.J. Preparation and Photocatalytic Mechanism of Vanadium Doped NaTaO<sub>3</sub> Nanoparticles. *Integr. Ferroelectr.* **2011**, *127*, 106–115.
44. Gao, R.; Zhou, S.X.; Li, W.; Chen, M.; Wu, L.M. Facile synthesis of uniform and well-defined single-crystal sodium tantalate cubes and their assembly into oriented two-dimensional nanofilm. *Cryst. Eng. Commun.* **2012**, *14*, 7031–7035.
45. Grewe, T.; Meier, K.; Tuysuz, H. Photocatalytic hydrogen production over various sodium tantalates. *Catal. Today* **2014**, *225*, 142–148.
46. Wang, X.J.; Bai, H.L.; Meng, Y.; Zhao, Y.H.; Tang, C.H.; Gao, Y. Synthesis and Optical Properties of Bi<sup>3+</sup> Doped NaTaO<sub>3</sub> Nano-Size Photocatalysts. *J. Nanosci. Nanotechnol.* **2010**, *10*, 1788–1793.
47. Liu, Y.L.; Su, Y.G.; Han, H.; Wang, X.J. Hydrothermal Preparation of Copper Doped NaTaO<sub>3</sub> Nanoparticles and Study on the Photocatalytic Mechanism. *J. Nanosci. Nanotechnol.* **2013**, *13*, 853–857.
48. Sardar, K.; Petrucco, E.; Hiley, C.I.; Sharman, J.D.B.; Wells, P.P.; Russell, A.E.; Kashtiban, R.J.; Sloan, J.; Walton, R.I. Water-Splitting Electrocatalysis in Acid Conditions Using Ruthenate-Iridate Pyrochlores. *Angew. Chem. Int. Edit.* **2014**, *53*, 10960–10964.
49. Müller-Buschbaum, H. On the crystal chemistry of Oxoiridates. *Z. Anorg. Allg. Chem.* **2005**, *631*, 1005–1028.
50. Kato, H.; Kudo, A. Highly efficient decomposition of pure water into H<sub>2</sub> and O<sub>2</sub> over NaTaO<sub>3</sub> photocatalysts. *Catal. Lett.* **1999**, *58*, 153–155.
51. Kumada, N.; Morozumi, Y.; Yonesaki, Y.; Takei, T.; Kinomura, N.; Hayashi, T. Preparation of Na<sub>0.5</sub>Bi<sub>0.5</sub>TiO<sub>3</sub> by hydrothermal reaction. *J. Ceram. Soc. Jap.* **2008**, *116*, 1238–1240.
52. Handoko, A.D.; Goh, G.K.L.; Chew, R.X. Piezoelectrically active hydrothermal KNbO<sub>3</sub> thin films. *Cryst. Eng. Commun.* **2012**, *14*, 421–427.
53. O'Brien, A.; Woodward, D.I.; Sardar, K.; Walton, R.I.; Thomas, P.A. Inference of oxygen vacancies in hydrothermal Na<sub>0.5</sub>Bi<sub>0.5</sub>TiO<sub>3</sub>. *Appl. Phys. Lett.* **2012**, *101*, 142902.
54. Singh, H.P. Determination of thermal expansion of germanium, rhodium and iridium by X-rays. *Acta Crystallogr. Sect. A* **1968**, *24*, 469–471.
55. Kanhere, P.; Zheng, J.; Chen, Z. Visible light driven photocatalytic hydrogen evolution and photophysical properties of Bi<sup>3+</sup> doped NaTaO<sub>3</sub>. *Int. J. Hydro. Ener.* **2012**, *37*, 4889–4896.

56. Onishi, H. Sodium Tantalate Photocatalysts Doped with Metal Cations: Why Are They Active for Water Splitting? *ChemSusChem* **2019**, *12*, 1825–1834.
57. Alves, G.A.S.; Centurion, H.A.; Sambrano, J.R.; Ferrer, M.M.; Gonçalves, R.V. Band Gap Narrowing of Bi-Doped NaTaO<sub>3</sub> for Photocatalytic Hydrogen Evolution under Simulated Sunlight: A Pseudocubic Phase Induced by Doping. *ACS Appl. Energy Mater.* **2021**, *4*, 671–679.
58. Suzuki, S.; Matsumoto, H.; Iwase, A.; Kudo, A. Enhanced H<sub>2</sub> evolution over an Ir-doped SrTiO<sub>3</sub> photocatalyst by loading of an Ir cocatalyst using visible light up to 800 nm. *Chem. Commun.* **2018**, *54*, 10606–10609.